PERGAMON

International Journal of Solids and Structures 40 (2003) 3393–3423

INTERNATIONAL JOURNAL OF SOLIDS and STRUCTURES

www.elsevier.com/locate/ijsolstr

An implicit algorithm for hypoelasto-plastic and hypoelasto-viscoplastic endochronic theory in finite strain isotropic–kinematic-hardening model

A.R. Khoei *, A. Bakhshiani, M. Mofid

Department of Civil Engineering, Sharif University of Technology, P.O. Box. 11365-9313, Tehran, Iran

Received 8 August 2002; received in revised form 21 February 2003

Abstract

This paper is concerned with objective stress update algorithm for elasto-plastic and elasto-viscoplastic endochronic theory within the framework of additive plasticity. The elastic response is stated in terms of hypoelastic model and endochronic constitutive equations are stated in unrotated frame of reference. A trivially incrementally objective integration scheme for rate constitutive equations is established. Algorithmic modulus consistent with numerical integration algorithm of constitutive equations is extracted. The implementation is validated by means of a set of simple deformation paths (simple shear, extension and rotation), two benchmark test in nonlinear mechanics (the necking of a circular bar and expansion of a thick-walled cylinder), a test which demonstrates the capabilities of the proposed model in simulation of cyclic loading and ratcheting in finite strain case (cyclically loaded notched bar) and finally, the analysis of a tensile test, which presents a shear band with a finite thickness independent of the finite element mesh using endochronic viscoplastic constitutive model.

Keywords: Endochronic theory; Viscoplasticity; Hypoelastic model; Large strain; Stress update

1. Introduction

The main objective of this paper is the formulation and integration of the endochronic constitutive equations for finite deformation metal plasticity and viscoplasticity. The endochronic theory deals with the plastic response of materials by means of memory integrals, expressed in terms of memory kernels. Formulation of this theory is based on thermo dynamical concepts and provides a unified point of view to describe the elastic–plastic behavior of material, since it places no requirement for a yield surface and 'loading function' to distinguish between loading and unloading. A key ingredient of the theory is that the deformation history is defined with respect to a deformation memory scale called intrinsic time. In the

* Corresponding author. Tel.: +98-21-6005818; fax: +98-21-6014828.
E-mail address: arkhoei@sharif.edu (A.R. Khoei).

0020-7683/03/$ - see front matter © 2003 Elsevier Science Ltd. All rights reserved.
doi:10.1016/S0020-7683(03)00155-0

original version of the endochronic theory, proposed by Valanis (1971a,b), the intrinsic time was defined as the path length in the total strain space. The so-called endochronic theory violates the second law of thermodynamics and leads to constitutive relations, which characterize inherently unstable materials (Rivlin, 1981; Sandler, 1978). Aiming at the correction of this deficiency, a new version of the endochronic theory was developed by Valanis (1980) in which the intrinsic time was defined as the path length in the plastic strain space. The new endochronic plasticity was capable of predicting a stress-response to deformation processes, including reversal points in loading in agreement with the experimentally observed mechanical behavior of metals. Also, Valanis demonstrated that an introduction of Dirac delta function into the kernel function leads to a derived result of a yield surface and classical plasticity models of isotropic and kinematic hardening could be derived as a special case of the endochronic theory (Valanis, 1980).

Using original endochronic theory, as a point of departure, a method of extending endochronic theory to concrete, clay and sand was proposed by Bazant and his coworkers (Bazant and Krizek, 1976; Bazant and Bhat, 1976; Bazant et al., 1979) by introducing sensitivity of intrinsic time to hydrostatic pressure and incorporating inelastic dilatancy due to shear strain. But the proposed approach has shortcomings of the original endochronic theory mentioned above. An extension of the new endochronic theory to concrete and sand was proposed by Valanis et al. (Valanis and Read, 1986; Valanis and Peters, 1991) and Wu et al. (1985). Recently, Khoei and Bakhshiani (2001) and Khoei et al. (2002) developed an endochronic theory to describe the behavior of metal powder in powder compaction processes.

The first implementation of an endochronic theory into a multi-dimensional finite element code was made by Lin et al. (1981), who focused on the original endochronic theory with one term exponential for the kernel function. An implicit finite element algorithm for the modern version of endochronic theory without a yield surface was developed by Valanis and Fan (1984), which was incrementally nonlinear. Also, Watanbe and Atluri (1985) presented an implicit finite element algorithm for the modern endochronic theory. They used the endochronic plasticity with yield surface and the resulting constitutive equations were incrementally linear. An unconditional stable integration scheme of endochronic constitutive equations was proposed by Hsu et al. (1991) and Hsu and Griffin (1992) and its ability is examined in the modeling of random non proportional tests on OFHC copper. Hsu and Griffin (1996) implemented radial return algorithm in integration of endochronic constitutive equations and applied their formulation to finite element micromechanics modeling of a unidirectional metal matrix composite subjected to nonproportional cyclic loading.

The endochronic theory has also been extended to investigate the rate dependent behavior of materials. Lin and Wu (1976) used original version of the endochronic theory and introduced a rate sensitivity function, which was a function of total strain rate. Wu and Yip (1980) redefined the rate sensitivity function of intrinsic time measure based on the new intrinsic time proposed by Valanis (1980) and discussed the uniaxial stress–strain responses of 1100-O aluminum and mild steel at constant strain rate conditions. Wu and Ho (1995) introduced another functional form for dependency of intrinsic time scale to the equivalent deviatoric plastic strain rate and applied endochronic theory to investigate transient creep of material. A new formulation of the rate sensitivity function was proposed by Pan and Chern (1997) to describe the viscoplastic behavior of material subjected to multiaxial loading. Pan (1997) modified the rate sensitivity function proposed by Pan and Chern (1997) and Pan et al. (1996) to incorporate with the finite endochronic constitutive equations. For the case of study, the finite simple torsion of iron and nickle thin-walled tubes were simulated with explicit constitutive equations. Pan et al. (1999) proposed a different formulation of the scaling function of the intrinsic time measure, as suggested originally by Valanis (1975), to describe the material behavior under rate dependent elastoplastic deformation. They used the differential endochronic constitutive equations derived by Valanis (1984) to describe the material responses subjected to rate dependent elastoplastic deformation.

The endochronic theory was extended to finite deformation with the concept of the corotational rate and plastic spin by Im and Atluri (1987). They derived the governing equations by using the isoclinic configu-

ration as the intermediate configuration and the corresponding second Piola-Kirchhoff stress tensor. Cases of finite uniaxial compression and torsion were discussed in their work. Wu et al. (1995) incorporated the concepts of corotational rate, corotational integral and plastic spin to endochronic theory and applied it to description of rigid-plastic deformation in thin-walled tubes subjected to finite torsion. Pan et al. (1996) extended the ordinary differential constitutive equations of endochronic theory to simulate elastoplastic deformation in the range of finite strain using the concept of corotational rate. Different objective rates were incorporated into the theory and cases involving metal tubes under torsion and metal rectangular block under biaxial compression were discussed. Recently, an endochronic plasticity theory was developed by Khoei et al. (2003a) and Bakhshiani et al. (2003) to describe the large deformation in finite strain using the concepts of corotational stress rate and the additive decomposition of deformation rate. They derived the constitutive equations for thin-walled tube under torsion to simulate the axial effects for various materials subjected to simple and pure torsional loading. More recently, Bakhshiani et al. (2002a,b) and Khoei et al. (2003b,c) developed a density-dependent endochronic theory based on coupling between deviatoric and hydrostatic behavior in finite strain plasticity to simulate the compaction process of powder material.

In this paper, the infinitesimal theory of endochronic plasticity is extended to large strain range on the basis of the additive decomposition of the strain rate tensor and hypoelasticity. This approach is rather different with respect to the multiplicative decomposition of the deformation gradient, which is based on the work of Lee (1969) and used in numerous recent papers (Simo, 1988a,b; Eterovic and Bathe, 1990; Eve and Reddy, 1994; Fish and Shek, 2000; Ibrahimbegovic and Chorfi, 2000; Ponthot, 2002). The proposed integration algorithm treats the elastoplastic and the elasto-viscoplatic cases in a unified way. Constitutive equations are stated in unrotated frame of reference that greatly simplifies endochronic constitutive relations in finite plasticity and yields the efficiency of the presented algorithm by total uncoupling material and geometrical non linearities. An implicit scheme is employed in this article which is the efficient method for the type of nonlinear problems considered in this paper (Ponthot, 2002; Simo, 1988b). An integration scheme, which is accurate, stable and amenable to consistent linearization, is developed. Although the major challenge in the integration of rate constitutive equations in large deformation analysis is to achieve incremental objectivity, it has been trivially achieved in the proposed algorithm. Algorithmic modulus consistent with numerical integration of constitutive equations for endochronic theory is extracted. The implementation of consistent modulus in global tangent stiffness matrix is essential in preserving the quadratic rate of convergence of Newoton procedure in solving the equilibrium equations (Simo and Taylor, 1985). The efficiency of the proposed constitutive model and computational algorithms is demonstrated by several numerical examples.

This paper is organized as follows: in Section 2, we describe the endochronic plasticity model. In Section 3, the implementation of endochronic plasticity model in large deformation is introduced. Section 4 is devoted to numerical integration of constitutive equations. In Section 5, the consistent tangent modulus, which has an important role in the convergence rate of global nonlinear system of equations, is extracted. Section 6 is devoted to the assessment of the model and computational procedure. Finally, some concluding remarks are made in Section 7.

2. Endochronic constitutive model

Constitutive equations of the endochronic theory for rate-dependent, plastically incompressible, initially isotropic material is as follows:

$$\boldsymbol{\sigma}_{\mathrm{dev}} = 2\int_0^z \Phi(z-z')\frac{\mathrm{d}\boldsymbol{\varepsilon}^{\mathrm{p}}}{\mathrm{d}z'}\,\mathrm{d}z' \tag{1}$$

where $\Phi(z)$ is material function, called hereditary function. A time scale 'ς' is introduced which is independent of elapsed time, but intrinsically dependent on the deformation of material. It is through this parameter that history effects are introduced into constitutive equations of endochronic theory.

$$d\varsigma^2 = d\boldsymbol{\varepsilon}^p : d\boldsymbol{\varepsilon}^p \tag{2}$$

$$dz = \frac{d\varsigma}{f(\varsigma, \dot{\varsigma})} \tag{3}$$

where $f(\varsigma, \dot{\varsigma})$ denotes a material function, called scale function, which is a function of time scale ς, and its rate $\dot{\varsigma}$. In order to describe the viscoplastic material behavior, the rate sensitivity is introduced in scale function through rate of time scale. It should be mentioned that the so-called consistency viscoplastic model (Wang et al., 1997) can be derived as special case of the proposed model by introducing Dirac delta function to the hereditary function.

In above equations, the total stress tensor is denoted by $\boldsymbol{\sigma}$ and its deviatoric and hydrostatic parts by $\boldsymbol{\sigma}_{dev}$ and σ_h, respectively. The symbol $\boldsymbol{\varepsilon}$ represent the total strain tensor by deviatoric and volumetric parts $\boldsymbol{\varepsilon}_{dev}$ and ε_{vol}, respectively. The superscripts 'e' and 'p' indicate the elastic and plastic components, respectively.

As shown by Valanis (1980), the kernel function $\Phi(z)$ can be expressed in terms of a Dirichlet series, i.e.,

$$\Phi(z) = \sum_{r=1}^{\infty} A_r e^{-\alpha_r z} \tag{4}$$

with the requirements that A_r and α_r are nonnegative for all values of 'r', and the condition,

$$\sum_{r=1}^{\infty} \frac{A_r}{\alpha_r} < \infty \tag{5}$$

This condition ensures the integrability of $\Phi(z)$ over a finite domain of time scale 'z'. In numerical application, m-term Dirichlet series can be used as, (Hsu et al., 1991)

$$\Phi(z) = \sum_{r=1}^{m} A_r e^{-\alpha_r z} \tag{6}$$

The role of scale function $f(\varsigma, \dot{\varsigma})$ is crucial in the behavior of model. By scaling intrinsic time, this function causes hardening or softening plastic behavior as functions of time scale and its rate.

Although the yield surface has not been explicitly assumed in the endochronic theory, introducing Dirac delta to kernel functions, results implicitly this concept (Valanis, 1980). The above endochronic model contains various isotropic and kinematic hardening rules for special cases (Watanbe and Atluri, 1986), depending on the choice of the scale function $f(\varsigma, \dot{\varsigma})$ and the kernel $\Phi(z)$. Prager's linear kinematic hardening rule can be obtained if Dirac delta function and one constant term are used in kernel function. Introducing another exponential term to the kernel function results in the Armstrong and Frederick nonlinear kinematic hardening rule.

3. Implementation in large deformation

In finite deformation plasticity, there are generally two approaches. The first class of methods is based on hyperelastic–plastic relations, multiplicative elastic–plastic kinematics and the existence of Helmholtz free energy density governed by either elastoplastic deformation (Nemat-Nasser, 1979; Simo, 1988a), or elastic deformation solely (Eve and Reddy, 1994). The second class of methods is based on hypoelastic–plastic relations, additive decomposition of rate of deformation and the use of objective stress rates. Even though this formulation is very attractive from the computational point of view (Belytschko, 1983; Ponthot, 2002),

it is limited to small elastic strain in which the hypothesis of hypoelasticity is valid. This approach is appropriate for most engineering materials, including metals, where elastic strain remains small.

In this section, the hypoelasto-plastic formulation is presented in the context of finite deformation problem involving large strain. The constitutive model is stated in the unrotated frame of reference (Johnson and Bammann, 1984; Fish and Shek, 2000; Ponthot, 2002), in which it is simple to achieve incremental objectivity and also in the unrotated reference frame all constitutive models are cast regardless of finite rotations. This greatly simplifies the numerical implementation of endochronic constitutive model.

3.1. Kinematics

A material point in reference configuration Ω_0 with position vector X occupies position x at time t in deformed configuration Ω. So we have $x = \varphi(X,t)$. The motion from the original configuration to the deformed configuration has the deformation gradient $\mathbf{F}$ given by

$$\mathbf{F} = \frac{\partial x}{\partial X} \tag{7}$$

Applying polar decomposition theorem to $\mathbf{F}$

$$\mathbf{F} = \mathbf{V}\mathbf{R} = \mathbf{R}\mathbf{U} \tag{8}$$

where $\mathbf{V}$ and $\mathbf{U}$ are the left and right symmetric, positive definite stretch tensors, respectively, and $\mathbf{R}$ is a proper orthogonal tensor. The velocity gradient is denoted by $\mathbf{L}$ and may be expressed as

$$\mathbf{L} = \frac{\partial v}{\partial x} = \dot{\mathbf{F}}\mathbf{F}^{-1} \tag{9}$$

$$v = \frac{\mathrm{d}\varphi(X,t)}{\mathrm{d}t} \tag{10}$$

The velocity gradient can be written in terms of symmetric $\mathbf{D}$ and antisymmetric $\mathbf{W}$ parts, respectively, called rate of deformation ant spin tensors, as

$$\mathbf{L} = \mathbf{D} + \mathbf{W} \tag{11}$$

The unrotated rate of deformation tensor used in the next sections is defined as,

$$\widehat{\mathbf{D}} = \mathbf{R}^{\mathrm{T}}\mathbf{D}\mathbf{R} \tag{12}$$

The finite elastoplastic kinematics, which we use in this study, is based on additive decomposition of rate of deformation as (Nemat-Nasser, 1982),

$$\mathbf{D} = \mathbf{D}^{\mathrm{e}} + \mathbf{D}^{\mathrm{p}} \tag{13}$$

or in unrotated frame as,

$$\widehat{\mathbf{D}} = \widehat{\mathbf{D}}^{\mathrm{e}} + \widehat{\mathbf{D}}^{\mathrm{p}} \tag{14}$$

3.2. Hypoelastic–viscoplastic constitutive equations

Hypoelastic material law relates the rate of stress to the rate of deformation. A general form of the hypoelastic relation is given by

$$\boldsymbol{\sigma}^{\nabla} = f(\boldsymbol{\sigma}, \mathbf{D}) \tag{15}$$

where $\boldsymbol{\sigma}^{\nabla}$ represents any objective rate of Cauchy stress.

In literature many objective rates are introduced, such as: Jaumann, Truesdell and Green-Naghdi rates. Dienes (1979) has shown that there is spurious oscillation in the stress, which arises directly from the nature of the Jaumann rate. Vanishing of Truesdell rate does not ensure that the invariants of Cauchy stress tensor are constant (Johnson and Bammann, 1984), so in this case further plastic flow will exist. In this formulation, the constitutive model is posed in terms of Cauchy stress in unrotated configuration (Johnson and Bammann, 1984), as

$$\hat{\boldsymbol{\sigma}} = \mathbf{R}^{\mathrm{T}}\boldsymbol{\sigma}\mathbf{R} \tag{16}$$

The conjugate strain rate to $\hat{\boldsymbol{\sigma}}$ is $\widehat{\mathbf{D}}$ defined in Eq. (12). So the hypoelastic part of constitutive equation is

$$\dot{\hat{\boldsymbol{\sigma}}} = \boldsymbol{C}^{\mathrm{e}} : \widehat{\mathbf{D}}^{\mathrm{e}} \tag{17}$$

$$\widehat{\mathbf{D}} = \widehat{\mathbf{D}}^{\mathrm{e}} + \widehat{\mathbf{D}}^{\mathrm{p}} \tag{18}$$

where $\boldsymbol{C}^{\mathrm{e}}$ is the Hook stress–strain tensor given as

$$\boldsymbol{C}^{\mathrm{e}}_{ijkl} = K\delta_{ij}\delta_{kl} + 2\mu\left(\delta_{ik}\delta_{jl} - \tfrac{1}{3}\delta_{ij}\delta_{kl}\right) \tag{19}$$

where K and μ are the bulk and shear modulus of material, respectively.

In order to complete the hypoelasto-viscoplastic constitutive equation in the context of finite deformation plasticity, the endochronic constitutive equations in unrotated frame is presented as follows:

$$\hat{\boldsymbol{\sigma}}_{\mathrm{dev}} = 2\int_0^z \Phi(z - z')\frac{\widehat{\mathbf{D}}^{\mathrm{p}}}{\dot{z}'}\,\mathrm{d}z' \tag{20}$$

$$\dot{z} = \frac{\dot{\varsigma}}{f(\varsigma, \dot{\varsigma})} \tag{21}$$

$$\dot{\varsigma}^2 = \widehat{\mathbf{D}}^{\mathrm{p}} : \widehat{\mathbf{D}}^{\mathrm{p}} \tag{22}$$

where

$$\hat{\boldsymbol{\sigma}} = \hat{\boldsymbol{\sigma}}_{\mathrm{dev}} + \hat{\sigma}_{\mathrm{h}}\mathbf{I} \tag{23}$$

$$\hat{\boldsymbol{\sigma}}_{\mathrm{dev}} = \mathrm{dev}[\hat{\boldsymbol{\sigma}}] \tag{24}$$

$$\hat{\sigma}_{\mathrm{h}} = \tfrac{1}{3}\mathrm{tr}[\hat{\boldsymbol{\sigma}}] \tag{25}$$

and $\mathrm{dev}[\cdot] = [\cdot] - \frac{1}{3}\mathrm{tr}[.]\mathbf{I}$ with $\mathbf{I}$ as spatial metric tensor.

4. Numerical integration of constitutive equations

The major challenge in the integration of the rate constitutive equations in finite strain context is to achieve incremental objectivity. Using objective stress rates in constitutive equations results in objective formulation only in the limit of very small time step (Hughes and Winget, 1980). While the standard time discretization procedures do not lead in incremental objectivity, one efficient way to overcome this problem is to state constitutive equations in corotational frame. Assuming that the variables of the model at step n and the incremental displacement field $\Delta u = {}^{n+1}x - {}^{n}x$ at load step $n+1$ are known, the update of different variables of the model at load step $n+1$ is done as described. The left superscript refers to load step. Subsequently, the left superscript is omitted for current step.

Using polar decomposition $\mathbf{F} = \mathbf{R}\mathbf{U}$, relations (9) and (12) leads to

$$\widehat{\mathbf{D}} = \mathbf{R}^{\mathrm{T}}\mathbf{D}\mathbf{R} = \tfrac{1}{2}(\dot{\mathbf{U}}\mathbf{U}^{-1} + \mathbf{U}^{-1}\dot{\mathbf{U}}) \tag{26}$$

Midpoint rule results to

$$\widehat{\mathbf{D}}\Delta t = \tfrac{1}{2}(\Delta\mathbf{U}\,{}^{n+\frac{1}{2}}\mathbf{U}^{-1} + {}^{n+\frac{1}{2}}\mathbf{U}^{-1}\Delta\mathbf{U}) \tag{27}$$

where $\Delta\mathbf{U}$ and ${}^{n+\frac{1}{2}}\mathbf{U}$ in the above relation are

$$\Delta\mathbf{U} = {}^{n+1}\mathbf{U} - {}^{n}\mathbf{U} \tag{28}$$

$${}^{n+\frac{1}{2}}\mathbf{U} = \tfrac{1}{2}({}^{n+1}\mathbf{U} + {}^{n}\mathbf{U}) \tag{29}$$

The corotational increment of $\mathbf{D}$ is given as,

$$\Delta\hat{\mathbf{d}} = \Delta t\widehat{\mathbf{D}} = \tfrac{1}{2}(\Delta\mathbf{U}\,{}^{n+\frac{1}{2}}\mathbf{U}^{-1} + {}^{n+\frac{1}{2}}\mathbf{U}^{-1}\Delta\mathbf{U}) \tag{30}$$

Applying the backward Euler scheme to Eq. (17) yields

$$\hat{\boldsymbol{\sigma}} = {}^{n}\hat{\boldsymbol{\sigma}} + \boldsymbol{C}^{\mathrm{e}} : \widehat{\mathbf{D}}^{\mathrm{e}}\Delta t \tag{31}$$

$$\Delta\hat{\boldsymbol{\sigma}} = \boldsymbol{C}^{\mathrm{e}} : \Delta\hat{\mathbf{d}}^{\mathrm{e}} = \boldsymbol{C}^{\mathrm{e}} : (\Delta\hat{\mathbf{d}} - \Delta\hat{\mathbf{d}}^{\mathrm{p}}) \tag{32}$$

The other part of numerical scheme is the numerical integration of endochronic constitutive equations. Substituting Eq. (6) to (20), gives

$$\hat{\boldsymbol{\sigma}}_{\mathrm{dev}} = 2\sum_{r=1}^{m}\int_{0}^{z} A_r \mathrm{e}^{-\alpha_r(z-z')}\frac{\widehat{\mathbf{D}}^{\mathrm{p}}}{\dot{z}'}\,\mathrm{d}z' \tag{33}$$

In order to integrate Eq. (33) numerically, the loading is divided into n steps, thus

$$\hat{\boldsymbol{\sigma}}^{r}_{\mathrm{dev}}({}^{n}z) = 2\sum_{k=1}^{n}\frac{A_r}{\alpha_r}\frac{{}^{k}(\Delta\hat{\mathbf{d}}^{\mathrm{p}})}{{}^{k}\Delta z}[\mathrm{e}^{-\alpha_r({}^{n}z-{}^{k}z)} - \mathrm{e}^{-\alpha_r({}^{n}z-{}^{k-1}z)}] \tag{34}$$

$$\hat{\boldsymbol{\sigma}}_{\mathrm{dev}}({}^{n}z) = \sum_{r=1}^{m}\hat{\boldsymbol{\sigma}}^{r}_{\mathrm{dev}}({}^{n}z) \tag{35}$$

It is worth mentioning that the striking feature of the above scheme is the direct integration of hereditary function. Such a procedure, in general leads to more accurate results with much smaller number of increments, and results in an exact solution to endochronic equations, if the material has no hardening effect and the deformation process traces a piecewise linear path in the plastic strain space (Hsu et al., 1991).

Eq. (34) can be simplified as

$$\hat{\boldsymbol{\sigma}}^{r}_{\mathrm{dev}}({}^{n}z) = \hat{\boldsymbol{\sigma}}^{r}_{\mathrm{dev}}({}^{n-1}z)\mathrm{e}^{-\alpha_r{}^{n}\Delta z} + 2\frac{A_r}{\alpha_r}\frac{{}^{n}(\Delta\hat{\mathbf{d}}^{\mathrm{p}})}{{}^{n}\Delta z}(1 - \mathrm{e}^{-\alpha_r{}^{n}\Delta z}) \tag{36}$$

Incremental form of endochronic constitutive equations can be obtained from Eq. (36) by taking step $n+1$ as current step. The incremental equations needed in the numerical modeling of initial strain are as follows

$$\Delta\hat{\boldsymbol{\sigma}}_{\mathrm{dev}} = \sum_{r=1}^{m}{}^{n}(\hat{\boldsymbol{\sigma}}^{r}_{\mathrm{dev}})(\mathrm{e}^{-\alpha_r\Delta z} - 1) + 2\frac{\Delta\hat{\mathbf{d}}^{\mathrm{p}}}{\Delta z}\sum_{r=1}^{m}\frac{A_r}{\alpha_r}(1 - \mathrm{e}^{-\alpha_r\Delta z}) \tag{37}$$

$$\Delta\hat{\boldsymbol{\sigma}}_{\mathrm{dev}} = 2\mu(\Delta\hat{\mathbf{d}} - \Delta\hat{\mathbf{d}}^{\mathrm{p}}) \tag{38}$$

$$\Delta\varsigma^2 = \Delta\hat{\mathbf{d}}^{\mathrm{p}} : \Delta\hat{\mathbf{d}}^{\mathrm{p}} \tag{39}$$

$$\Delta z = \frac{\Delta\varsigma}{f\left({}^{n}\varsigma + \beta\Delta\varsigma, \frac{\Delta\varsigma}{\Delta t}\right)} \tag{40}$$

where β is a parameter with the condition $\beta \geqslant 1/2$. Although this set of six algebraic equations can be solved for the unknowns $(\Delta\hat{\mathbf{d}}^{\mathrm{p}})$ by applying the Newton–Raphson method, however, more efficient numerical scheme can be devised by making a few algebraic manipulations. Substituting $\Delta\hat{\boldsymbol{\sigma}}_{\mathrm{dev}}$ from (38) to (37) yields

$$2\mu\Delta\hat{\mathbf{d}} - \sum_{r=1}^{m} {}^{n}(\hat{\boldsymbol{\sigma}}^{r}_{\mathrm{dev}})(\mathrm{e}^{-\alpha_r\Delta z} - 1) = 2\frac{\Delta\hat{\mathbf{d}}^{\mathrm{p}}}{\Delta z}\left(\sum_{r=1}^{m}\frac{A_r}{\alpha_r}(1 - \mathrm{e}^{-\alpha_r\Delta z}) + \mu\Delta z\right) \tag{41}$$

Taking inner product of (41) with itself, results

$$\mathbf{A} : \mathbf{A} = B^2\frac{\Delta\varsigma^2}{\Delta z^2} \tag{42}$$

where

$$\mathbf{A}_{ij} = \mu\Delta\hat{\mathbf{d}}_{ij} - \frac{1}{2}\sum_{r=1}^{m} {}^{n}(\hat{\boldsymbol{\sigma}}^{r}_{\mathrm{dev}})_{ij}(\mathrm{e}^{-\alpha_r\Delta z} - 1) \tag{43}$$

and

$$B = \mu\Delta z + \sum_{r=1}^{m}\frac{A_r}{\alpha_r}(1 - \mathrm{e}^{-\alpha_r\Delta z}) \tag{44}$$

Substituting (40) into (42) gives

$$R(\Delta\varsigma) = \mathbf{A} : \mathbf{A} - B^2 f^2\left({}^{n}\varsigma + \beta\Delta\varsigma, \frac{\Delta\varsigma}{\Delta t}\right) = 0 \tag{45}$$

The above equation can be solved for $\Delta\varsigma$ by the Newton–Raphson technique using the following expression for derivative of residual with respect to unknown, $\Delta\varsigma$

$$\frac{\partial R}{\partial\Delta\varsigma} = 2\frac{\partial\mathbf{A}}{\partial\Delta\varsigma} : \mathbf{A} - 2fB\left(\frac{\partial B}{\partial\Delta\varsigma}f + B\frac{\partial f}{\partial\Delta\varsigma}\right) \tag{46}$$

$$\frac{\partial\mathbf{A}}{\partial\Delta\varsigma} = \frac{1}{2}\frac{\partial\Delta z}{\partial\Delta\varsigma}\sum_{r=1}^{m}\alpha_r^n(\hat{\boldsymbol{\sigma}}^{r}_{\mathrm{dev}})\mathrm{e}^{-\alpha_r\Delta z} \tag{47}$$

$$\frac{\partial B}{\partial\Delta\varsigma} = \frac{\partial\Delta z}{\partial\Delta\varsigma}\left(\mu + \sum_{r=1}^{m} C_r\mathrm{e}^{-\alpha_r\Delta z}\right) \tag{48}$$

$$\frac{\partial\Delta z}{\partial\Delta\varsigma} = \frac{1}{f} - \frac{\Delta\varsigma}{f^2}\frac{\partial f}{\partial\Delta\varsigma} \tag{49}$$

$$\frac{\partial f\left({}^{n}\varsigma + \beta\Delta\varsigma, \frac{\Delta\varsigma}{\Delta t}\right)}{\partial\Delta\varsigma} = \beta\frac{\partial f}{\partial\varsigma} + \frac{1}{\Delta t}\frac{\partial f}{\partial\dot{\varsigma}} \tag{50}$$

Once Eq. (45) is solved for $\Delta\varsigma$, Δz can be obtained from (40) and $\Delta\hat{\mathbf{d}}^{\mathrm{p}}$ from Eq. (41). Then the corotational increment of stress tensor is derived from Eq. (32). Stress is then calculated from relations $\hat{\boldsymbol{\sigma}} = {}^{n}\hat{\boldsymbol{\sigma}} + \Delta\hat{\boldsymbol{\sigma}}$ and $\boldsymbol{\sigma} = \mathbf{R}\hat{\boldsymbol{\sigma}}\mathbf{R}^{\mathrm{T}}$.

It can be seen from Eq. (27) that the proposed scheme is trivially incrementally objective. In the case of rigid body motion, ${}^{n+1}\mathbf{U} = {}^{n}\mathbf{U}$ and from Eq. (27) $\widehat{\mathbf{D}} = 0$, thus stress tensor will be updated exactly by relation ${}^{n+1}\boldsymbol{\sigma} = \Delta\mathbf{R}\,{}^{n}\boldsymbol{\sigma}\Delta\mathbf{R}^{\mathrm{T}}$. It should be mentioned that in this scheme the rotation tensor $\mathbf{R}$ is exactly computed from the polar decomposition and not from the numerical integration of rate equation $\dot{\omega} = \boldsymbol{\Omega}\omega$, with $\boldsymbol{\Omega}$ denoting a spin tensor and ω indicating an orthogonal rotation tensor.

5. Consistent tangent operator

In order to achieve the quadratic rate of convergence of Newton method for solution of global nonlinear system of equations, it is essential to use tangent modulus consistent with integration procedure of constitutive equations in forming tangent stiffness matrix (Simo and Taylor, 1985). In this section, the incremental constitutive equations derived in previous section are linearized to yield consistent tangent modulus.

Taking material time derivative of Eq. (37) yields

$$\Delta\dot{\hat{\boldsymbol{\sigma}}}_{\mathrm{dev}} = \mathbf{H}_1\Delta\dot{z} + H_2\Delta\dot{\hat{\mathbf{d}}}^{\mathrm{p}} \tag{51}$$

where

$$\mathbf{H}_1 = 2\frac{\Delta\hat{\mathbf{d}}^{\mathrm{p}}}{\Delta z}\sum_{r=1}^{m} A_r \mathrm{e}^{-\alpha_r\Delta z} - 2\frac{\Delta\hat{\mathbf{d}}^{\mathrm{p}}}{\Delta z^2}\sum_{r=1}^{m}\frac{A_r}{\alpha_r}(1-\mathrm{e}^{-\alpha_r\Delta z}) - \sum_{r=1}^{m}\alpha_r{}^{n}(\hat{\sigma}^{r}_{\mathrm{dev}})\mathrm{e}^{-\alpha_r\Delta z} \tag{52}$$

$$H_2 = \frac{2}{\Delta z}\sum_{r=1}^{m}\frac{A_r}{\alpha_r}(1-\mathrm{e}^{-\alpha_r\Delta z}) \tag{53}$$

Taking material time derivative of (40) yields

$$\Delta\dot{z} = \left(\frac{1}{f} - \frac{\Delta\varsigma}{f^2}\left(\beta\frac{\partial f}{\partial\varsigma} + \frac{1}{\Delta t}\frac{\partial f}{\partial\dot{\varsigma}}\right)\right)\Delta\dot{\varsigma} \tag{54}$$

where $\Delta\dot{\varsigma}$ can be obtained by taking time derivative from Eq. (39) which yields,

$$\Delta\dot{\varsigma} = \frac{1}{\Delta\varsigma}\Delta\hat{\mathbf{d}}^{\mathrm{p}} : \Delta\dot{\hat{\mathbf{d}}}^{\mathrm{p}} \tag{55}$$

Substituting Eqs. (54) and (55) to (51) yields

$$\Delta\dot{\hat{\boldsymbol{\sigma}}}_{\mathrm{dev}} = \boldsymbol{C}^{\mathrm{p}} : \Delta\dot{\hat{\mathbf{d}}}^{\mathrm{p}} \tag{56}$$

where

$$\boldsymbol{C}^{\mathrm{p}} = \frac{1}{\Delta\xi}\left(\frac{1}{f} - \frac{\Delta\varsigma}{f^2}\left(\beta\frac{\partial f}{\partial\varsigma} + \frac{1}{\Delta t}\frac{\partial f}{\partial\dot{\varsigma}}\right)\right)\mathbf{H}_1 \otimes \Delta\mathbf{d}^{\mathrm{p}} + H_2\boldsymbol{I} \tag{57}$$

Taking time derivative of (23) and using (19), (38) and (56) by straightforward calculation yields,

$$\dot{\hat{\boldsymbol{\sigma}}} = \overline{\boldsymbol{C}}^{\mathrm{p}} : \Delta\dot{\hat{\mathbf{d}}} \tag{58}$$

where

$$\overline{\boldsymbol{C}}^{\mathrm{p}} = \boldsymbol{C}^{\mathrm{e}}\left(\boldsymbol{I} - \left(\frac{1}{2\mu}\boldsymbol{C}^{\mathrm{p}} + \boldsymbol{I}\right)^{-1}\boldsymbol{I}^{\mathrm{dev}}\right) \tag{59}$$

and

$$\boldsymbol{I}^{\mathrm{dev}}_{ijkl} = \tfrac{1}{2}(\delta_{ik}\delta_{jl} + \delta_{il}\delta_{jk}) - \tfrac{1}{3}\delta_{ij}\delta_{kl} \tag{60}$$

In order to complete derivation of consistent modulus, linearization of ${}^{n+1}\mathbf{R}$ and $\Delta\hat{\mathbf{d}}$ is needed. For consistent linearization of ${}^{n+1}\mathbf{R}$, we start by relation,

$$\mathbf{L} = \dot{\mathbf{F}}\mathbf{F}^{-1} = \mathbf{R}\mathbf{R}^{\mathrm{T}} + \mathbf{R}\dot{\mathbf{U}}\mathbf{U}^{-1}\mathbf{R}^{\mathrm{T}} \tag{61}$$

Pre-multiplying Eq. (61) with $\mathbf{R}^{\mathrm{T}}$ and post-multiplying with $\mathbf{F}$ yields,

$$\mathbf{R}^{\mathrm{T}}\mathbf{L}\mathbf{F} = \mathbf{R}^{\mathrm{T}}\dot{\mathbf{R}}\mathbf{U} + \dot{\mathbf{U}} \tag{62}$$

Subtracting (62) from its transpose after some manipulation results in

$$\dot{\mathbf{R}} = \boldsymbol{G} : \mathbf{L} \tag{63}$$

where

$$\boldsymbol{G}_{ijkl} = (\mathbf{R}_{im}\mathbf{U}_{jn} - \mathbf{R}_{in}\mathbf{U}_{jm})^{-1}(\mathbf{R}_{km}\mathbf{F}_{ln} - \mathbf{R}_{kn}\mathbf{F}_{lm}) \tag{64}$$

Substituting (63) to (62) gives $\dot{\mathbf{U}}$ in terms of $\mathbf{L}$ as follows,

$$\dot{\mathbf{U}} = \boldsymbol{H} : \mathbf{L} \tag{65}$$

where

$$\boldsymbol{H}_{ijkl} = (\mathbf{R}_{ki}\mathbf{F}_{lj} - \mathbf{R}_{mi}\mathbf{U}_{nj}\boldsymbol{G}_{mnkl}) \tag{66}$$

In order to evaluate $\Delta\dot{\hat{\mathbf{d}}}$ appearing in Eq. (58) consistent with integration scheme, relation (30) is used,

$$\dot{\hat{\mathbf{d}}} = \boldsymbol{P} : {}^{n+1}\dot{\mathbf{U}} \tag{67}$$

where

$$\boldsymbol{P}_{ijkl} = \tfrac{1}{2}({}^{n+\frac{1}{2}}\mathbf{U}^{-1}_{kj}\delta_{il} + {}^{n+\frac{1}{2}}\mathbf{U}^{-1}_{ik}\delta_{jl} - \tfrac{1}{2}\Delta\mathbf{U}_{im}\,{}^{n+\frac{1}{2}}\mathbf{U}^{-1}_{mk}\,{}^{n+\frac{1}{2}}\mathbf{U}^{-1}_{lj} - \tfrac{1}{2}\Delta\mathbf{U}_{mj}\,{}^{n+\frac{1}{2}}\mathbf{U}^{-1}_{ik}\,{}^{n+\frac{1}{2}}\mathbf{U}^{-1}_{lm}) \tag{68}$$

Substituting (65) to (67) yields,

$$\dot{\hat{\mathbf{d}}} = \widetilde{\boldsymbol{H}} : \mathbf{L} \tag{69}$$

where $\widetilde{\boldsymbol{H}}$ is a forth-order tensor given as

$$\widetilde{\boldsymbol{H}} = \boldsymbol{P} : \boldsymbol{H} \tag{70}$$

Substituting Eq. (69) into Eq. (58) yields

$$\dot{\hat{\boldsymbol{\sigma}}} = \boldsymbol{C} : \mathbf{L} \tag{71}$$

where

$$\boldsymbol{C}_{ijkl} = \overline{\boldsymbol{C}}^{\mathrm{p}}_{ijmn}\widetilde{\boldsymbol{H}}_{mnkl} \tag{72}$$

Combining Eqs. (63) and (71) and $\dot{\hat{\boldsymbol{\sigma}}} = \mathbf{R}^{\mathrm{T}}\dot{\boldsymbol{\sigma}}\mathbf{R} + \dot{\mathbf{R}}^{\mathrm{T}}\boldsymbol{\sigma}\mathbf{R} + \mathbf{R}^{\mathrm{T}}\boldsymbol{\sigma}\dot{\mathbf{R}}$ yields

$$\dot{\boldsymbol{\sigma}} = \widetilde{\boldsymbol{C}} : \mathbf{L} \tag{73}$$

where

$$\widetilde{\boldsymbol{C}}_{ijkl} = \mathbf{R}_{im}\boldsymbol{C}_{mnkl}\mathbf{R}_{jn} - \mathbf{R}_{im}\boldsymbol{G}_{nmkl}\boldsymbol{\sigma}_{nj} - \boldsymbol{\sigma}_{im}\boldsymbol{G}_{mnkl}\mathbf{R}_{jn} \tag{74}$$

6. Numerical simulation examples

In this section, several numerical simulations are presented to study the performance of the proposed formulation. The finite element mesh employed in all simulations is four-node isoparametric elements with bilinear displacement interpolation and constant pressure to handle the isochoric nature of plastic flow. The convergence criterion used is based on the relative value of norm of residual forces to norm of applied forces. Unless otherwise stated, the convergence tolerance is set to 10^{-4} and β is set to $1/2$.

6.1. Simple shear test

The first example is chosen to examine the behavior of model and accuracy of the numerical integration scheme in the case of large deformation. The problem statement for the simple shear test is shown in Fig. 1. Both elastic and elastoplastic behaviors are considered. The equations describing the motion of the continuum are

$$\begin{aligned} x(t) &= X + Yt \\ y(t) &= Y \end{aligned} \tag{75}$$

Elastic behavior is represented by Young's modulus of 2000 and Poisson's coefficient of 0.3. Figs. 2 and 3 present the results for the elastic case. The results of hypoelastic model with Green-Naghdi and Jaumann rates are also depicted for comparison. Both mid-point and fully implicit algorithms yield to sufficiently accurate results for shear strain response in relatively large increment (50% shear strain in each increment). Fully implicit algorithm grossly underestimates σ_{xx} component when not enough increments are employed, and demands a smaller strain increment to get accurate solution.

Endochronic plasticity model with kernel function parameters of $C_1 = 2000$, $C_2 = 200$, $r_1 = 100$, $r_2 = 10$ and scale function of $f(\varsigma) = 1 + (\varsigma/10)$ is employed for simulation of elastoplastic behavior. Mid-point numerical integration algorithm is used for this case. Fig. 4 shows shear stress response versus shear strain for three different time steps. It can be seen from this figure that the proposed integration algorithm results in acceptable solutions even in the case of large prescribed strain increments. Taking the solution at 5000 time steps, as the exact solution, the error in final shear stress corresponding to shear strain of 5 is computed and plotted versus the number of time increments in Fig. 5. From this figure, the second-order accuracy of the integration algorithm is corroborated.

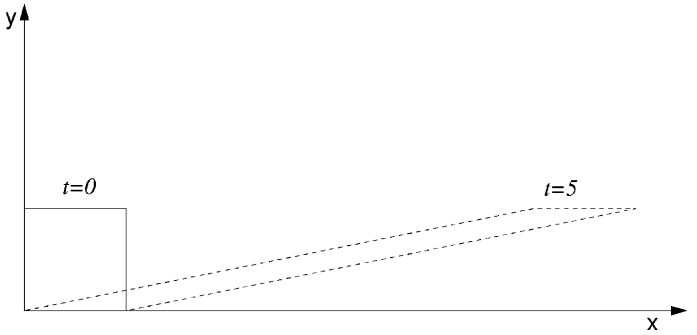

Fig. 1. Simple shear test; problem statement.

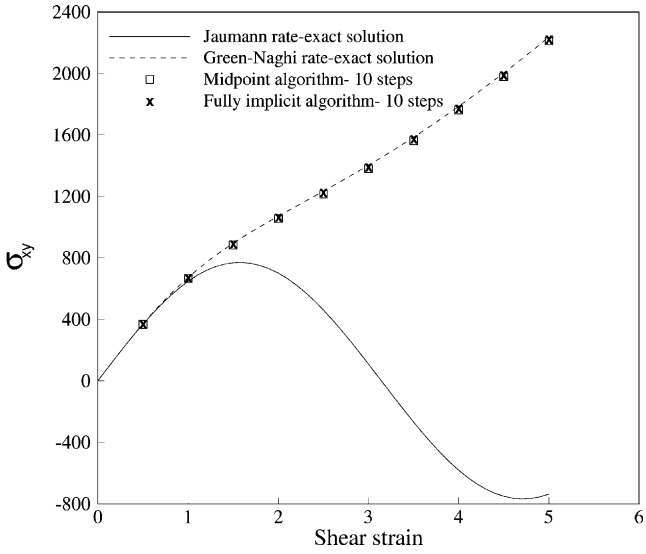

Fig. 2. Simple shear test; the stress component σ_{xy} versus shear strain in elastic analysis.

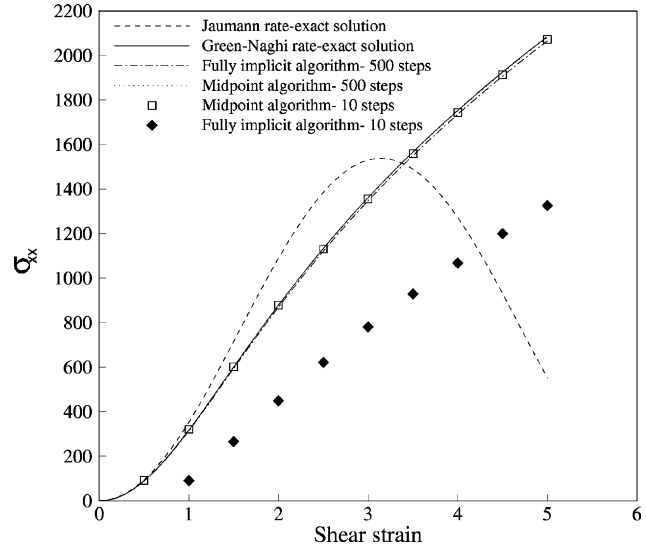

Fig. 3. Simple shear test; the stress component σ_{xx} versus shear strain in elastic analysis.

6.2. Extension and rotation test

In second example, a combined extension and rotation of an element is considered to illustrate the behavior of the kinematic algorithm and accuracy of the proposed integration scheme in the case of small deformation combined with large rigid body rotation. This example was made by Rashid (1993) to show that the algorithm of Hughes and Winget (1980) is the only weakly objective, which can cause unintended

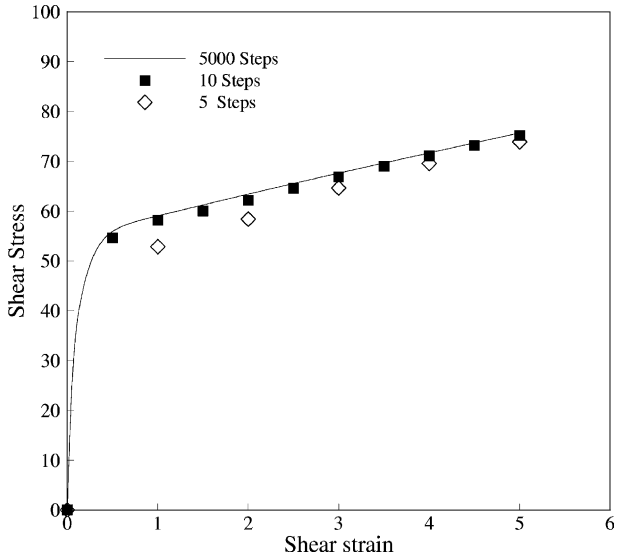

Fig. 4. Simple shear test; the shear stress versus shear strain in elasto-plastic analysis.

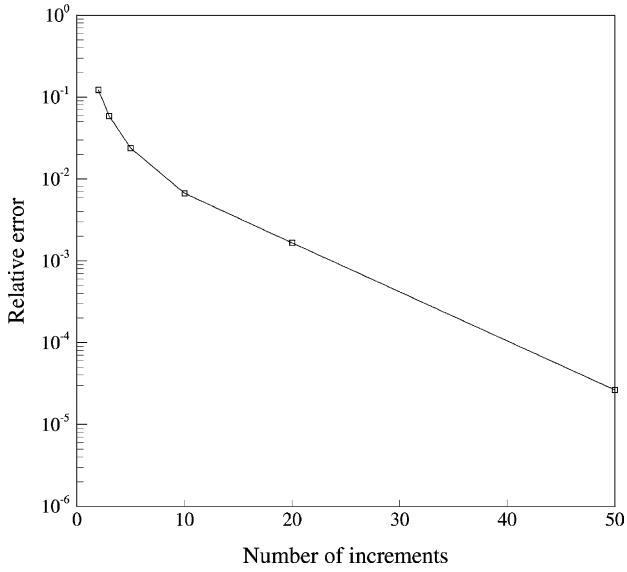

Fig. 5. Simple shear test; the error in final value of shear stress versus number of time steps in elasto-plastic analysis.

coupling between the rotational part of the motion and the stress update, whenever large rotational increments are present. This characteristic can cause inaccurate results in the case of large rotational increments.

The problem statement for this example is shown in Fig. 6. A unit square simultaneously undergoes a uniaxial extension of 0.005 and a total superposed rigid rotation of 90°. The equations of motion are

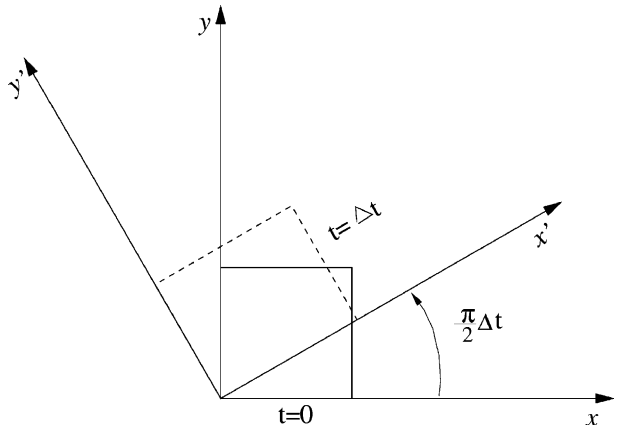

Fig. 6. Extension and rotation test; problem statement.

$$x(t) = X(1 + 0.005t)\cos\left(\frac{\pi}{2}t\right) - Y\sin\left(\frac{\pi}{2}t\right)$$
$$y(t) = X(1 + 0.005t)\sin\left(\frac{\pi}{2}t\right) + Y\cos\left(\frac{\pi}{2}t\right) \tag{76}$$

and the analytical solution is

$$\sigma_{xx} = \frac{Et}{400(1-\nu^2)}(1 + \cos\pi t)$$
$$\sigma_{yy} = \frac{Et}{400(1-\nu^2)}(1 - \cos\pi t) \tag{77}$$
$$\sigma_{xy} = \frac{Et}{400(1-\nu^2)}\sin\pi t$$

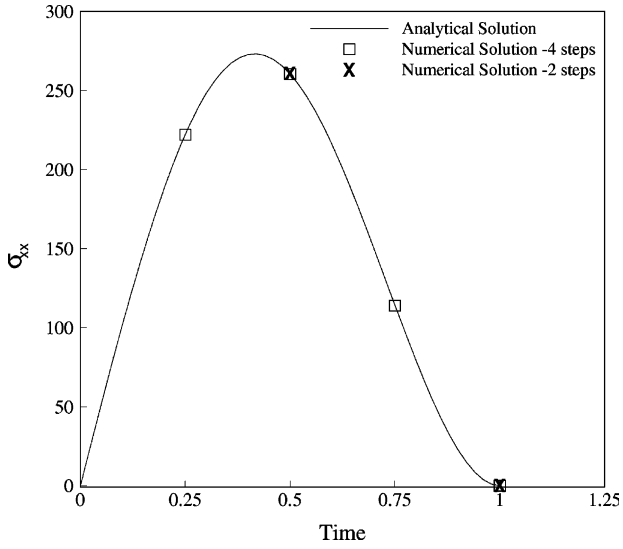

Fig. 7. Extension and rotation test; the stress component σ_{xx} versus time.

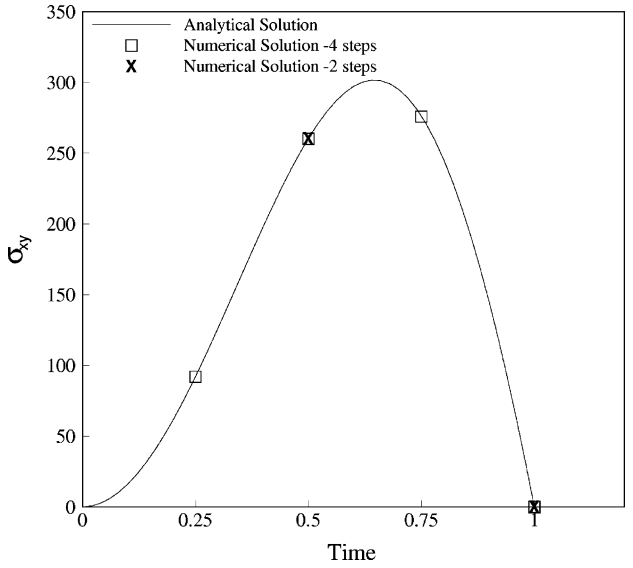

Fig. 8. Extension and rotation test; the stress component σ_{xy} versus time.

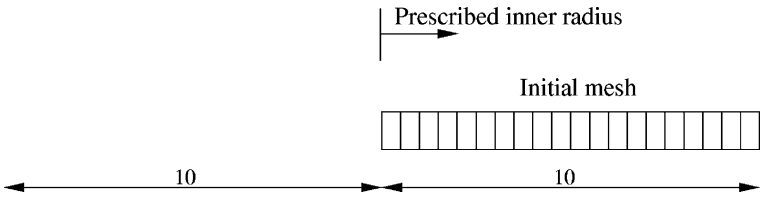

Fig. 9. Expansion of a thick-walled cylinder; geometry and initial mesh.

Table 1
Material properties for the thick-walled cylinder

Young's modulus	11 050 MPa
Poisson's ratio	0.454
C_1	180 000 MPa
C_2	90 000 MPa
r_1	30 000
r_2	10 000
Scale function	$f(\varsigma) = 0.0148$

The material Young's modulus E is taken as 200 000 and the Poisson's ratio is 0.2. The elastic behavior is only parameter considered here. The results of this example are shown in Figs. 7 and 8. It is clear that the predictions of the proposed algorithm agree with analytical values for large incremental rotation, even up to 45°.

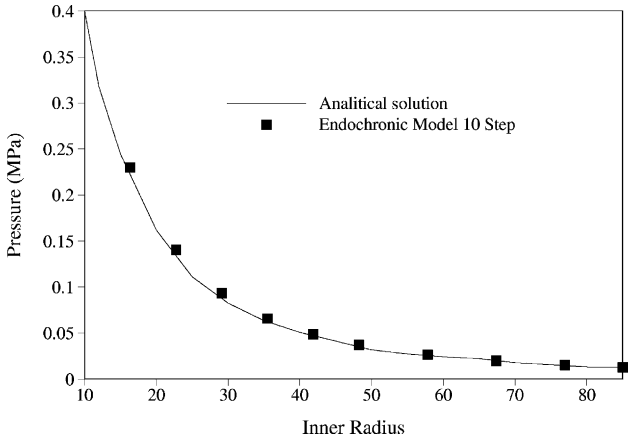

Fig. 10. Expansion of a thick-walled cylinder; the internal pressure versus inner radius.

6.3. Expansion of a thick-walled cylinder

The next example is one of the most popular benchmarks for validating finite plasticity formulation (Simo, 1988b; Fish and Shek, 2000; Ponthot, 2002). A thick-walled cylinder with an inner radius of 10 units and an outer radius of 20 units is subjected to internal pressure. This problem is solved using 20 bilinear axisymmetric elements. The convergence tolerance used for this example is 10^{-7}. Fig. 9 shows the finite element mesh and configuration of the cylinder. The inner radius is driven to a value of 90 in ten load steps. The endochronic material parameters, given in Table 1, are chosen to simulate the rigid-plastic behavior with the yield stress of 0.5 MPa allowing a comparison with analytical solution.

Fig. 10 shows the relationship between the inner radius and internal pressure. The radial stress profile versus position through current thickness of the cylinder is shown in Fig. 11. It can be seen that the numerical results are in good agreement with the analytical solution. Newton iterations per load step and

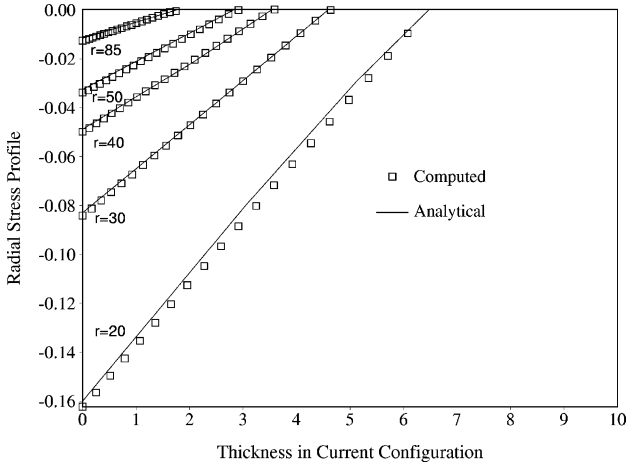

Fig. 11. Expansion of a thick-walled cylinder; the radial stress versus position relative to inner radius corresponding to several configurations.

Table 2
Newton iterations per load step, Example 6.3

Step	1	2	3	4	5–6	7	8–10
Number of iterations	9	8	7	6	5	6	5

Table 3
Residual norm for load steps 4 and 8, Example 6.3

Iteration	Load step 4	Load step 8
1	1.69E+03	3.20E+03
2	2.15E+01	2.43E+01
3	2.54E−01	1.23E−01
4	2.75E−03	6.23E−04
5	2.94E−05	8.37E−08
6	2.47E−08	

values of residual norm during iterations of two typical time steps are given in Tables 2 and 3, respectively, which demonstrate the quadratic rate of asymptotic convergence.

6.4. Cyclically loaded notched bar

This example is chosen to demonstrate the capabilities of endochronic plasticity in simulation of cyclic loading and ratcheting. An axisymmetric notched bar is subjected to cyclic displacement and stress loadings. The geometry and finite element mesh of the problem are shown in Fig. 12. This example was considered by Kobayashi and Ohno (2002) to show the behavior of a new form of kinematic hardening

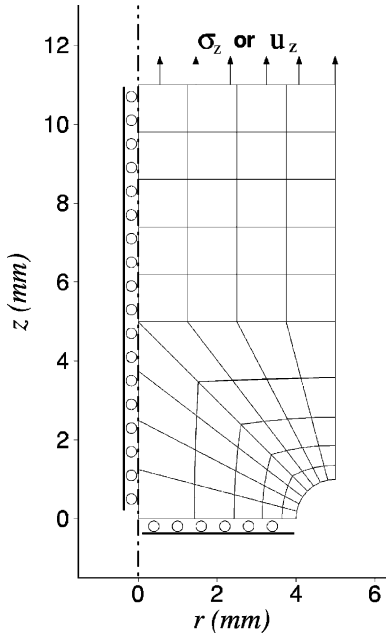

Fig. 12. Geometry, finite element mesh and boundary condition of notched bar subjected to cyclic loading.

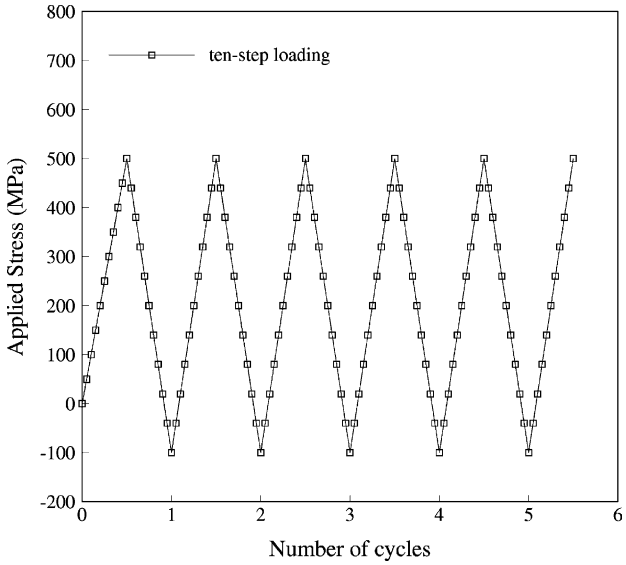

Fig. 13. Cyclically loaded notched bar; cyclic loading diagram and increment of applied axial stress.

Table 4
Material properties for the cyclically loaded notched bar

Young's modulus	165 000 MPa
Poisson's ratio	0.3
C_1	200 000 MPa
C_2	4000 MPa
C_3	800 MPa
r_1	50 000
r_2	1000
r_3	50
Scale function	$f(\varsigma) = 35$

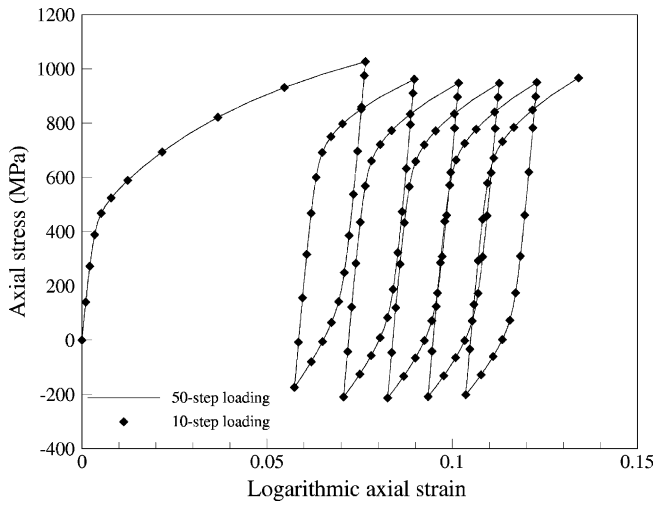

Fig. 14. Notched bar subjected to cyclic stress loading; the axial stress versus strain relation at the integration point near notch root.

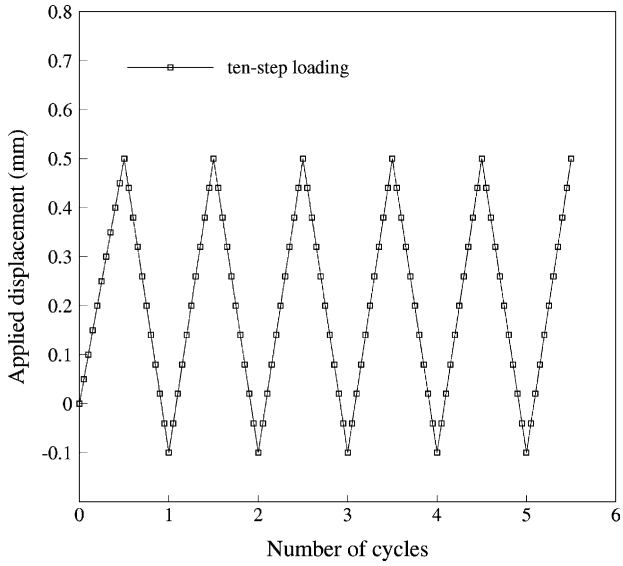

Fig. 15. Cyclically loaded notched bar; cyclic loading diagram and increment of applied axial displacement.

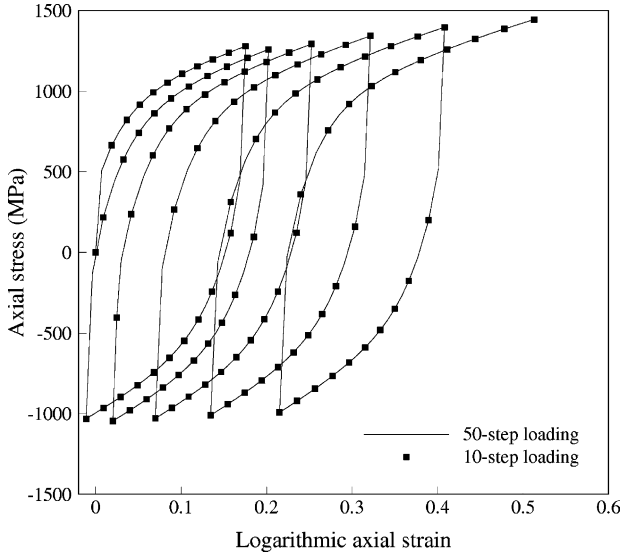

Fig. 16. Notched bar subjected to cyclic displacement loading; the axial stress versus strain relation at the integration point near notch root.

Table 5
Residual norm-stress loading, Example 6.4

Iteration	Last increment of third cycle	Tenth increment of fourth cycle	First increment of fifth cycle
1	1.64E+1	7.29E+1	2.20E+3
2	6.41E−1	3.83E−3	9.34E+2
3	2.08E−2	2.61E−6	2.70E+0
4	1.12E−4		3.83E−3
5			7.40E−7

plasticity in small displacement context. Fig. 13 illustrates the variation of applied stress with the number of cycles. The increment of applied stress is prescribed to allocate ten and fifty steps per half a cycle. Endochronic material parameters used for simulation are given in Table 4. Using a constant scale function suppresses, the isotropic hardening of model and three terms of kernel function are enough to simulate a nonlinear kinematic hardening behavior.

Table 6
Residual norm-displacement loading, Example 6.4

Iteration	Last increment of third cycle	Tenth increment of fourth cycle	First increment of fifth cycle
1	1.06E+0	2.15E+0	6.84E+4
2	1.06E−2	1.57E−2	5.68E+2
3	9.45E−5	5.60E−5	6.50E+0
4			1.52E−1
5			1.08E−2
6			1.82E−5

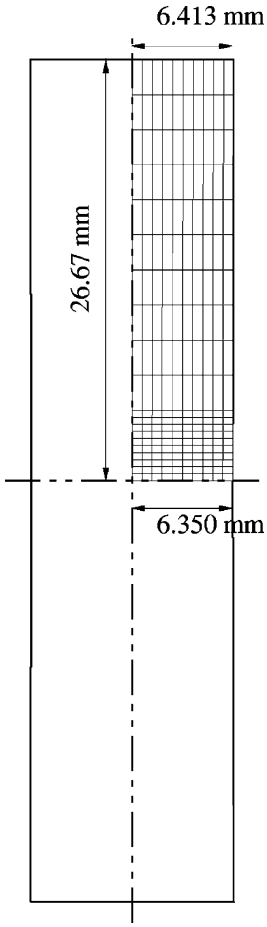

Fig. 17. Necking of a circular bar; problem description.

Fig. 14 shows the computed axial stress–strain relations at the integration point near the notch root. The capability of the endochronic model to simulate ratcheting is clear from the figure. Also, using only ten stress increments gives accurate results for such a complicated loading history. Fig. 15 shows cyclic loading diagram and the increment of applied displacement at the top of the specimen. Axial stress versus strain relation at the integration point near notch root is shown in Fig. 16. Similar to the previous loading case, ten steps loading per half a cycle is sufficient to obtain an accurate result. It is worth mentioning while the concepts of the yield surface and loading-unloading criteria have not been assumed in the endochronic plasticity, the model can effectively simulate unloading and cyclic loading. Finally, Tables 5 and 6 show the values of residual norm during iterations of three typical time step for the stress loading and displacement loading cases, respectively. The reported values of residuals are also given corresponding to ten steps loading per half cycle.

6.5. Necking of a circular bar

Necking phenomenon in a bar is a well-known test in nonlinear solid mechanics and has been considered by many researchers (Hallquist, 1983; Simo, 1988b; Rodriguez-Ferran et al., 1997; Ponthot, 2002). A circular bar, with a radius of 6.413 and 53.334 mm length, is subjected to uniaxial tension up to total axial elongation of 14 mm (Fig. 17). For an ideal case of a perfect specimen, necking can start in any section of

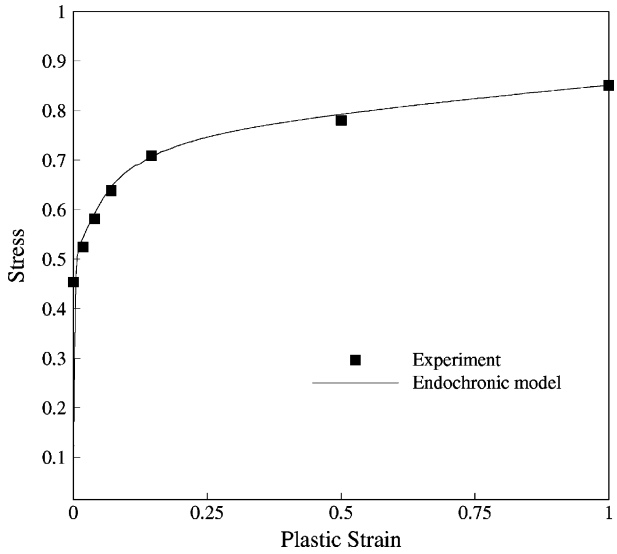

Fig. 18. Necking of a circular bar; uniaxial hardening curve.

Table 7
Material properties for the necking of a circular bar

Young's modulus	206.9 GPa
Poisson's ratio	0.29
C_1	168.6 GPa
r_1	400
Scale function	$f(\varsigma) = 0.69 - 0.21e^{-11\varsigma} + 0.16\varsigma$

specimen. In order to replace such a problem with multiple solutions by a problem with unique solution a geometric imperfection (1% radius reduction) is introduced to induce necking in the central part of the bar. Fig. 18 shows how the endochronic model can be fitted to experimental data, reported by Simo (1988b), which leads to the endochronic material parameters, given in Table 7.

Three different meshes, consisting of 50, 200 and 800 quadrilateral bilinear elements, corresponding to one quarter of specimen have been considered, as shown in Fig. 19, in order to assess the accuracy of discretization. The deformed finite element meshes after total 14 mm of axial elongation corresponding to one quarter of the specimen are shown in Fig. 20. The contours of the Cauchy stress components σ_{rr} and σ_{zz} for 800 elements mesh corresponding to 14 mm axial elongation are shown in Fig. 21. They are in good agreement with those reported by Simo (1988b) and Ponthot (2002).

A comparison between experimental and some computed results of the ratio of the current to initial radius at the necking section versus axial elongation is shown in Fig. 22. The result is in good agreement with experimental and other computed results. The sensitivity of numerical solution to mesh refinement is assessed in Fig. 23, where the necking ratio versus elongation is plotted for three meshes with 50, 200 and 800 elements. This figure corroborates the insensitivity of the numerical results to the mesh refinement. The sensitivity of the solution with respect to time discretization is examined in Fig. 24. It is noted that the results corresponding to 50 and 100 load steps are very similar, which confirms the accuracy of the integration scheme. In Tables 8 and 9, the computational efforts involved in the calculations are assessed. Table 8 summarizes the required number of iteration per load step for 50 element mesh. Also, the values of residual norm during iterations for two typical load steps are shown in Table 9.

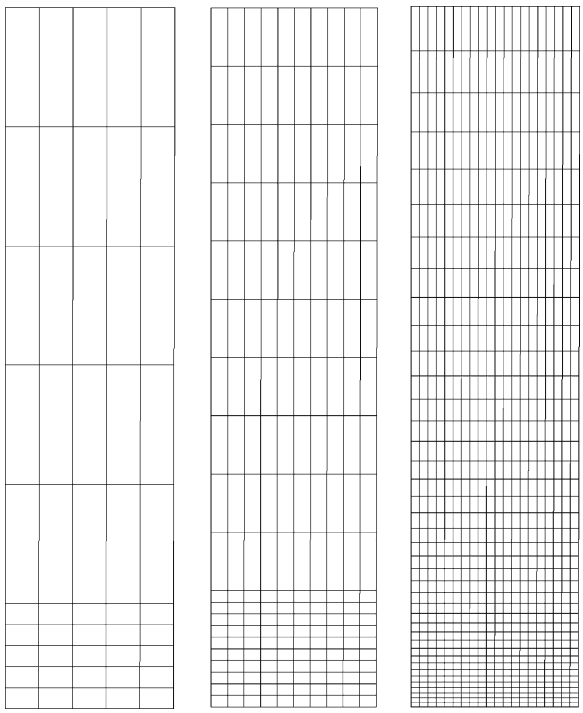

Fig. 19. Necking of a circular bar; finite element meshes corresponding to one quarter of the specimen, consisting of 50, 200 and 800 elements.

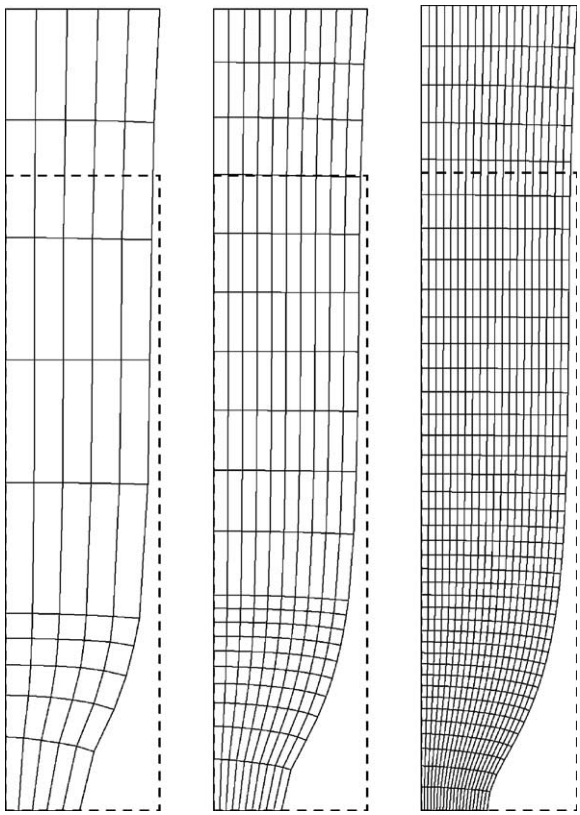

Fig. 20. Necking of a circular bar; finite element meshes after the total axial elongation of 14 mm corresponding to one quarter of the specimen, consisting of 50, 200 and 800 elements.

6.6. Strip in tension-shear banding

In the last example, the evolution of the shear band in a plane strain strip with strain softening endochronic plasticity is investigated and the capability of endochronic viscoplastic model in providing the mesh objective results is demonstrated. A strip is constrained at the bottom while a constant velocity of $v = 20$ mm/s is imposed at the top, as shown in Fig. 25. The Endochronic strain softening plasticity is used with material parameters given in Table 10. In order to avoid homogeneous solution, the width of specimen is slightly increased toward the top, so that the shear band will be initiated at the bottom right of the specimen. Two different meshes have been used with 200 and 400 bilinear quadrilateral plane strain elements.

It is well known that the strain softening will result in the mathematical ill posesness of field equations (Khoei et al., 1997; Khoei et al., 2003d). Because no length scale is involved in the evolution of shear band, the localization zone is confined to the size of element, which yields to mesh dependent results. Fig. 26 shows the displacement patterns and load deflection curves corresponding to two different meshes with endochronic softening plasticity. It is evident from the displacement patterns that the width of shear band is determined by the element size and the deformation is localized along a line of integration points. Also, the mesh dependency is obvious from the load deflection curves. It should be noted that the large deformation analysis can not solve the mesh dependency of solution. This lack of objectivity can be overcome by using

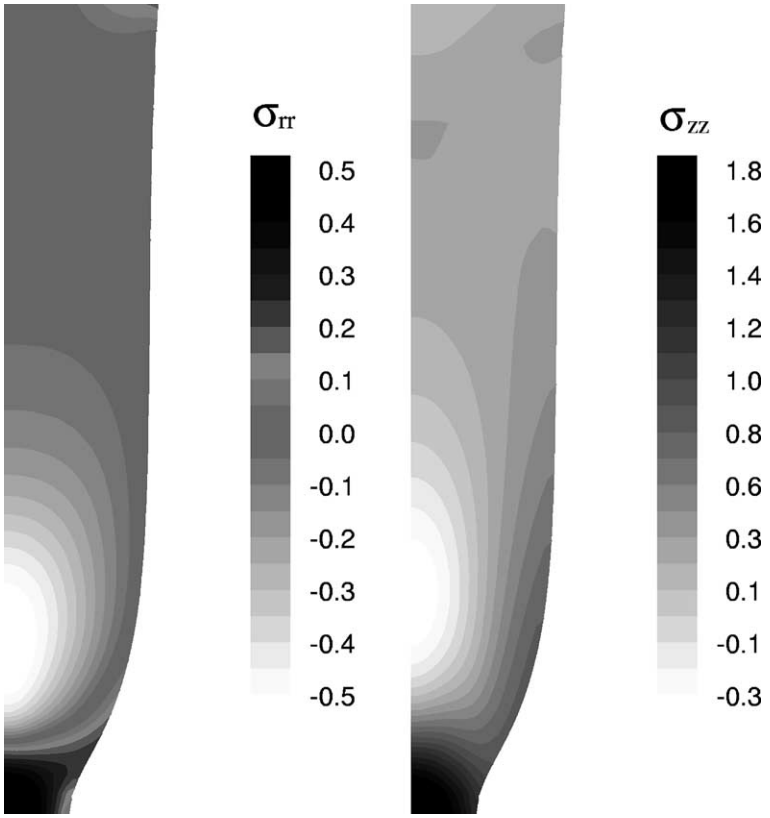

Fig. 21. Necking of a circular bar; the contours of Cauchy stress components σ_{rr} and σ_{zz} for 800 element mesh.

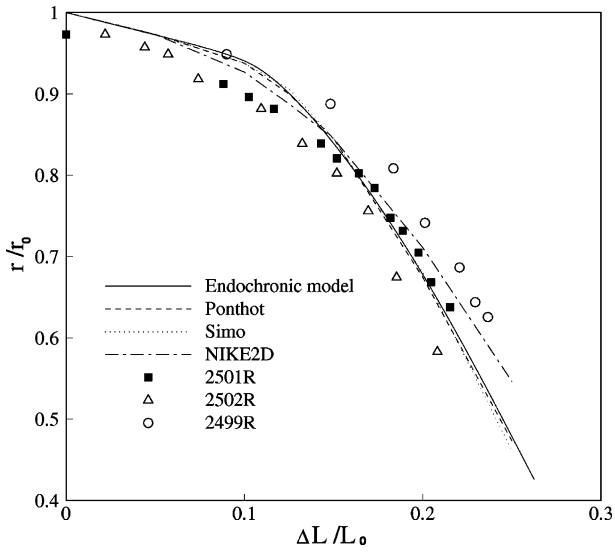

Fig. 22. Necking of a circular bar; the experimental and computed results of the ratio of current to initial radius at the section undergoing extreme necking versus axial elongation.

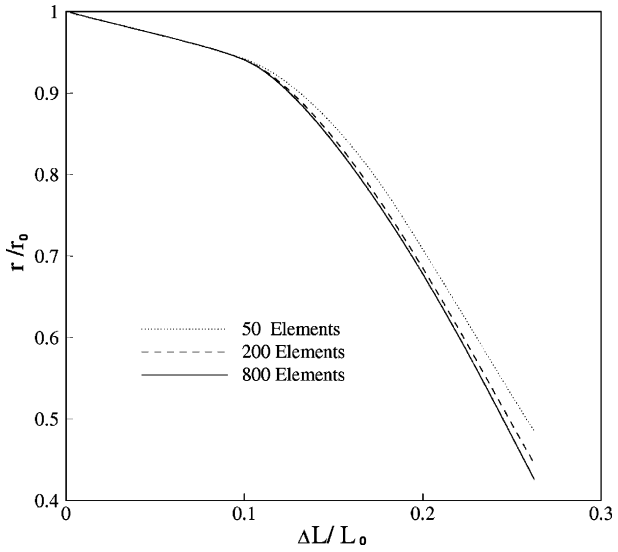

Fig. 23. Necking ratio versus axial elongation in necking of a circular bar; the sensitivity study of numerical calculation with respect to mesh refinement.

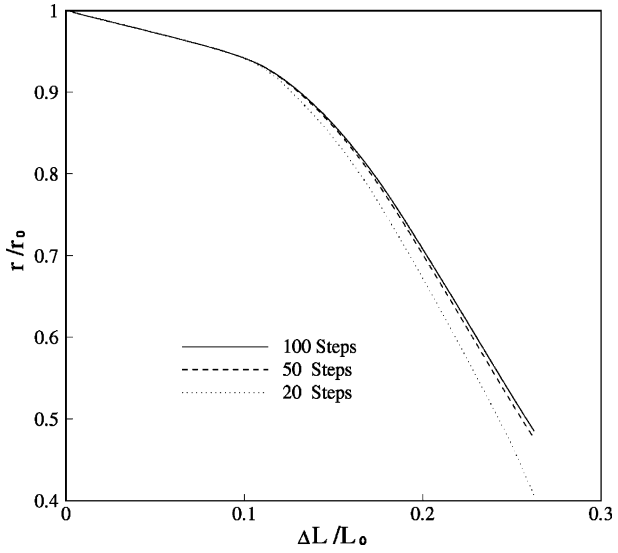

Fig. 24. Necking ratio versus axial elongation in necking of a circular bar; the accuracy of the integration algorithm for different load step sizes.

Table 8
Newton iterations per load step, Example 6.5

Step	1	2	3–4	5–7	8–13	14	15	16	17	18–21	22	23–30
Number of iterations	6	5	4	3	5	4	7	5	6	5	7	5

Table 9
Residual norm for load steps 14 and 28, Example 6.5

Iteration	Load step 14	Load step 28
1	2.98E+0	8.41E+0
2	1.71E−2	3.71E−1
3	7.70E−4	8.29E−2
4	2.03E−6	6.42E−3
5		1.41E−5

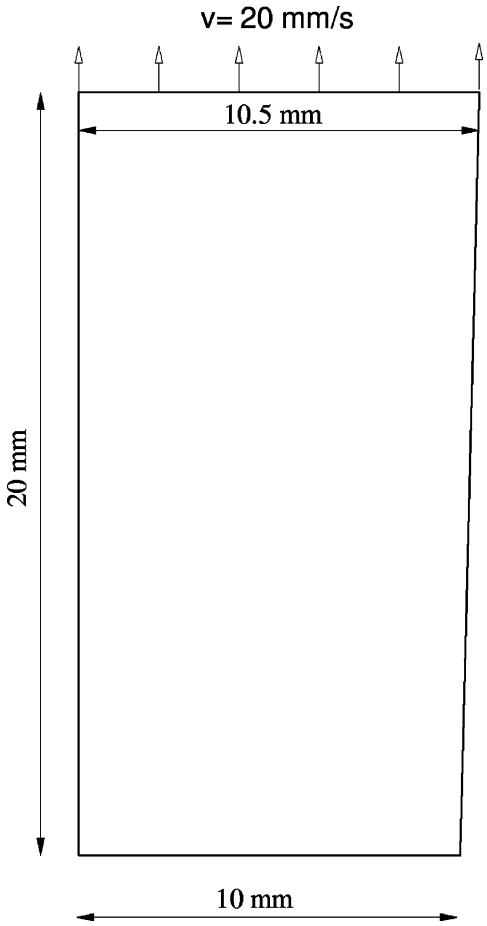

Fig. 25. Strip in tension; problem description.

Table 10
Material properties for the strip in tension

Young's modulus	30 000 MPa
Poisson's ratio	0.3
C_1	15 000 MPa
C_2	1500 MPa
r_1	10 000
r_2	4000
Scale function	$f(\varsigma) = 10(1 - 10\varsigma)$

the rate dependent viscoplastic model introducing a length scale into initial value problem (Needleman, 1988). Endochronic material parameters given in Table 10 are used, but additionally a linear viscosity term in the scale function is introduced:

$$f(\varsigma,\dot{\varsigma}) = 10(1 - 10\varsigma + 0.0125\dot{\varsigma}) \tag{78}$$

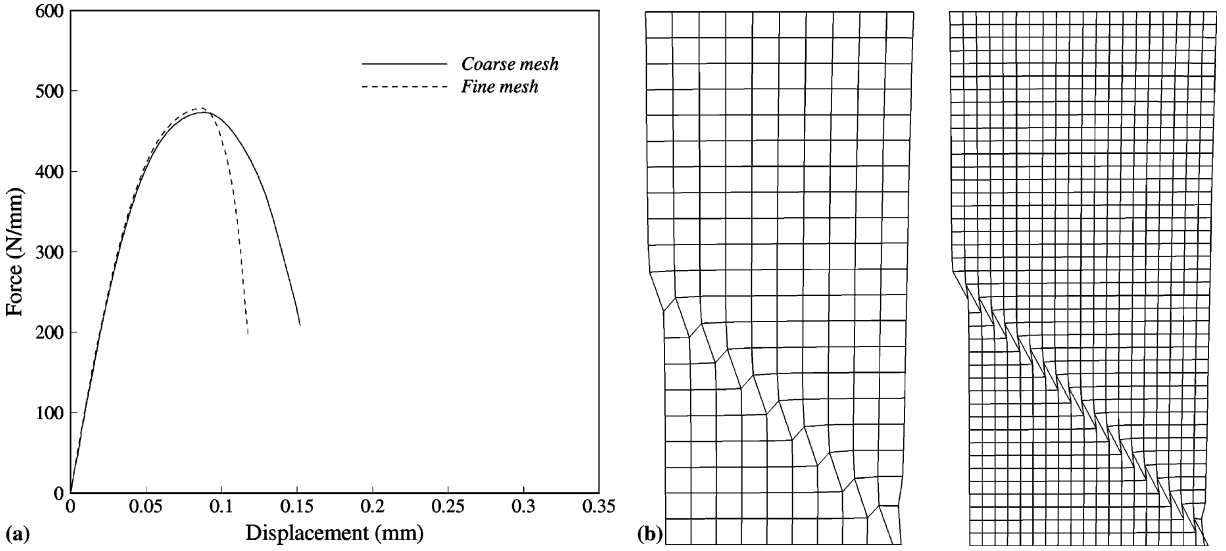

Fig. 26. Strip in tension; the mesh-dependent results with endochronic strain-softening plasticity; (a) load–deformation curves, (b) displacement patterns.

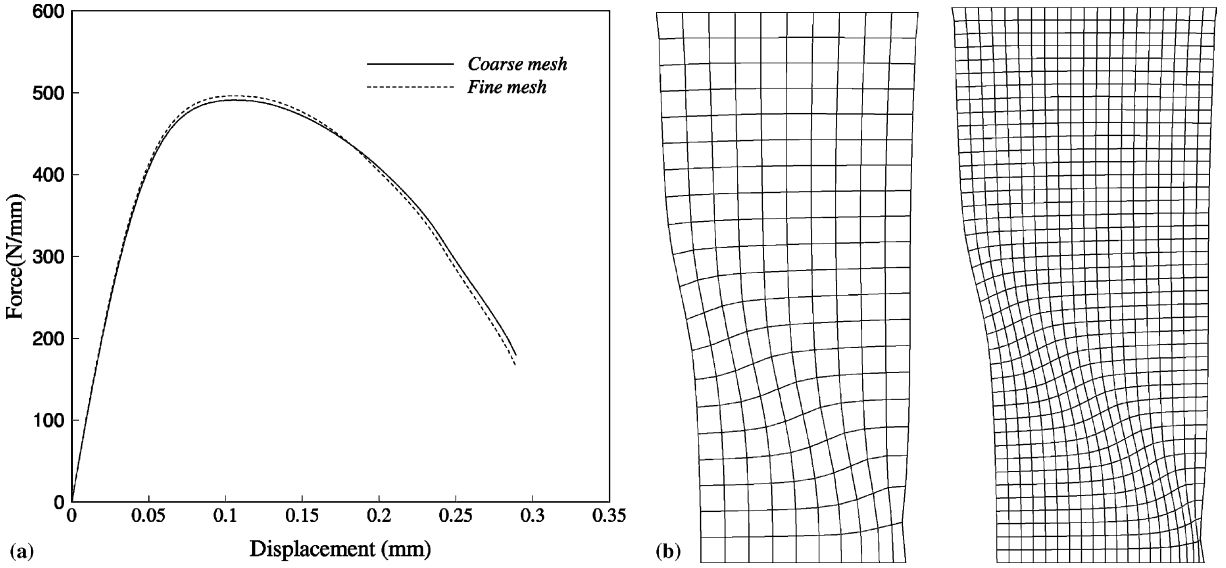

Fig. 27. Strip in tension; the mesh objective results with endochronic viscoplastic model; (a) load–deformation curves, (b) displacement patterns.

Fig. 27 shows the displacement patterns and load deflection curves of two different meshes using the endochronic viscoplastic model with scale function defined in (78). The finite width of the shear band and its independency of the finite element size can be observed. Also, similar load–deflection curves can be observed from two different meshes, which corroborates the mesh objectivity of results. Finally, contour plots of the equivalent plastic strain using endochronic plasticity and endochronic viscoplastic models for two different meshes are shown in Fig. 28.

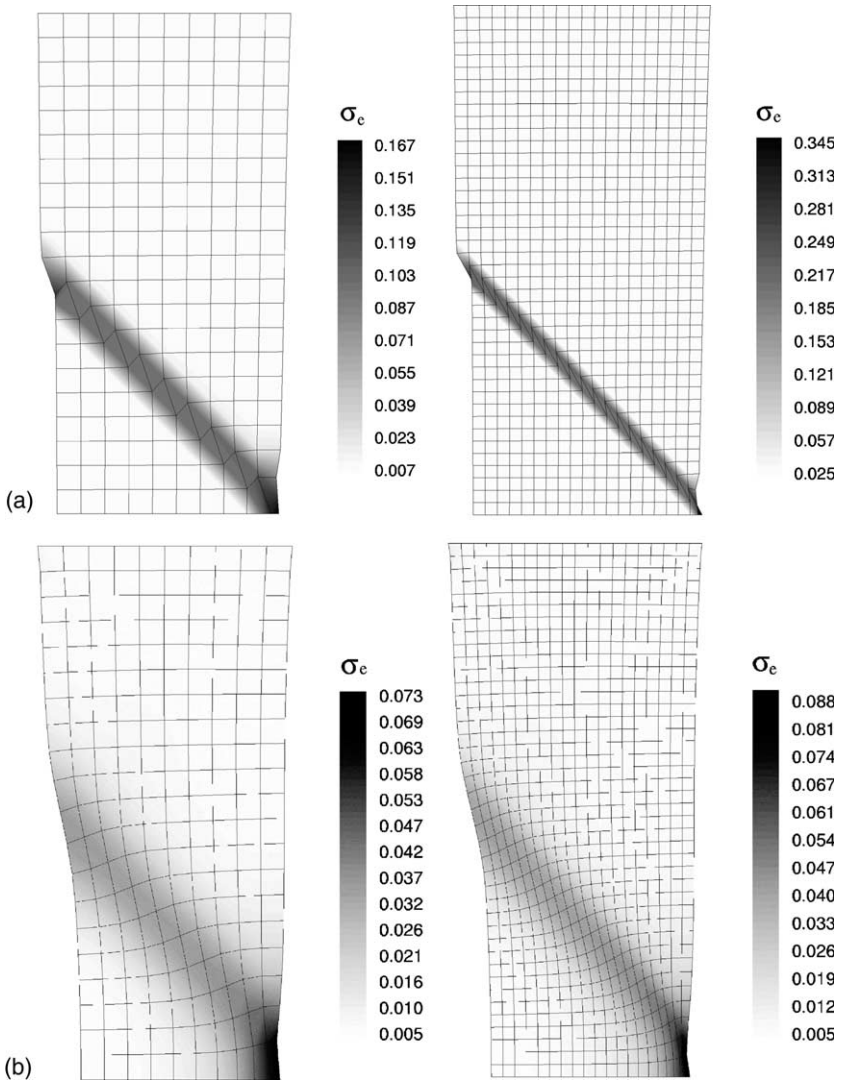

Fig. 28. Strip in tension; the equivalent plastic strain contours; (a) endochronic plasticity model for total extension of 20 mm, (b) endochronic viscoplastic model for total extension of 30 mm.

7. Conclusions

In the present paper, a computational framework was presented for the finite strain endochronic viscoplastic model, which is capable of accounting for both isotropic and kinematic hardening effects. The elastic response was stated in terms of hypoelastic model and the endochronic plasticity constitutive equations were stated in unrotated frame of reference. A trivially incrementally objective integration scheme was established for the rate constitutive relations and the algorithmic modulus consistent with numerical integration algorithm of constitutive equations was extracted. Numerical examples show a quadratic rate of global convergence even in the case of complicated applied loading path and relatively large load steps. The capability of the proposed model in simulation of cyclic loading and ratcheting in finite strain is demonstrated. The implementation is validated by means of a set of simple deformation paths and two benchmark tests in nonlinear mechanics. Finally, the analysis of a tensile test shows a shear band with a finite thickness independent of the finite element mesh using endochronic viscoplastic constitutive model.

References

Bakhshiani, A., Khoei, A.R., Mofid, M., 2002a. An endochronic plasticity model for powder compaction processes. J. Mater. Process. Technol. 125–126, 138–143.

Bakhshiani, A., Khoei, A.R., Mofid, M., 2002b. A density-dependent endochronic plasticity for powder compaction processes. Comput. Meth. Appl. Mech. Engng., submitted for publication.

Bakhshiani, A., Mofid, M., Khoei, A.R., McCabe, S.L., 2003. Finite strain simulation of thin-walled tube under torsion using endochronic theory of plasticity. Thin-Walled Struct. 41 (5), 435–459.

Bazant, Z.P., Bhat, P.D., 1976. Endochronic theory of inelasticity and failure of concrete. J. Engng. Mech. Div. ASCE 102, 701–722.

Bazant, Z.P., Krizek, R.J., 1976. Endochronic constitutive law for liquefaction of sand. J. Engng. Mech. Div. ASCE 102, 225–238.

Bazant, Z.P., Ansal, A.M., Krizek, R.J., 1979. Visco-plasticity of transversely isotropic clays. J. Engng. Mech. Div. ASCE 105, 549–565.

Belytschko, T., 1983. An overview of semidiscretization and time integration procedures. In: Belytschko, T., Hughes, T.J.R. (Eds.), Computational Methods for Transient Analysis. Elsevier Science Publisher, pp. 1–95.

Dienes, J.K., 1979. On the analysis of rotation and stress rate in deforming bodies. Acta Mech. 32, 217–232.

Eterovic, A., Bathe, K., 1990. A hyperelastic based large strain elasto-plastic constitutive formulation with combined isotropic–kinematic hardening using the logarithmic stress and strain measures. Comput. Meth. Appl. Mech. Engng. 30, 1099–1114.

Eve, R.A., Reddy, B.D., 1994. The variational formulation and solution of problems of finite strain elastoplasticity based on the use of dissipation function. Int. J. Numer. Meth. Engng. 37, 1673–1695.

Fish, J., Shek, K., 2000. Finite deformation plasticity based on additive split of the rate of deformation and hyperelasticity. Comput. Meth. Appl. Mech. Engng. 140, 75–93.

Hallquist, J., 1983. NIKE2D-a Vectorized implicit finite deformation finite element code for analyzing the static and dynamic response of 2D solids. Technical report UCID-19677. Lawrence Livermore National Laboratory, University of California.

Hsu, S.Y., Jain, S.K., Griffin, O.H., 1991. Verification of endochronic theory for non-proportional loading paths. ASCE J. Engng. Mech. 117, 110–131.

Hsu, S.Y., Griffin, O.H., 1992. On stability and efficiency of numerical integration of endochronic constitutive equations. Comput. Struct. 44, 657–665.

Hsu, S.Y., Griffin, O.H., 1996. Algorithmic tangent matrix approach for mixed hardening model of endochronic plasticity. Comput. Meth. Appl. Mech. Engng. 133, 1–14.

Hughes, T.J.R., Winget, J., 1980. Finite rotation effects in numerical integration of rate constitutive equations arising in large deformation analysis. Int. J. Numer. Meth. Engng. 15, 1862–1867.

Ibrahimbegovic, A., Chorfi, L., 2000. Viscoplasticity model at finite deformation with combined isotropic and kinematic hardening. Comput. Struct. 77, 509–525.

Im, S., Atluri, S.N., 1987. A study of two finite strain plasticity models: an internal time theory using Mandel's director concept and a general isotropic/kinematic hardening theory. Int. J. Plasticity. 3, 163.

Johnson, G.C., Bammann, D.J., 1984. A discussion of stress rates in finite deformation problems. Int. J. Solids Struct. 20, 725–737.

Khoei, A.R., Bakhshiani, A., 2001. Modeling of powder compaction using an endochronic plasticity model in finite element method. Seventh Europ. Conf. Adv. Mater. Process., Italy.

Khoei, A.R., Bakhshiani, A., Mofid, M., 2003a. Finite strain endochronic plasticity with reference to metal tube under torsion. Engng. Comput. 20 (3), 248–273.

Khoei, A.R., Bakhshiani, A., Mofid, M., 2003b. An endochronic plasticity model for finite strain deformation of powder forming processes. Finite Elem. Anal. Des., in press.

Khoei, A.R., Bakhshiani, A., Mofid, M., 2003c. An endochronic plasticity model for numerical simulation of industrial powder compaction processes. Commun. Numer. Meth. Engng. 19 (7), 521–534.

Khoei, A.R., Lewis, R.W., Zienkiewicz, O.C., 1997. Application of the finite element method for localized failure analysis in dynamic loading, Finite Elem. Anal. Des. 27, 121–131.

Khoei, A.R., Mofid, M., Bakhshiani, A., 2002. Modelling of powder compaction process using an endochronic plasticity model. J. Mater. Process. Technol. 130–131, 175–180.

Khoei, A.R., Tabarraie, A.R., Gharehbaghi, S.A., 2003d. *H*-adaptive mesh refinement for shear band localization in elasto-plasticity Cosserat continuum. Comput. Struct., submitted for publication.

Kobayashi, M., Ohno, N., 2002. Implementation of cyclic plasticity models based on a general form of kinematic hardening. Int. J. Numer. Meth. Engng. 53, 2217–2238.

Lee, E., 1969. Elastic–plastic deformation at finite strains. J. Appl. Mech. 36, 1–6.

Lin, H.C., Wu, H.C., 1976. Strain rate effect in the endochronic theory of viscoplasticity. J. Appl. Mech. 98, 92–96.

Lin, H.C., Hsieh, B.J., Valentin, R.A., 1981. The application of endochronic plasticity theory in modeling the dynamic inelastic response of structural systems. Nucl. Engng. Des. 66, 213–221.

Needleman, A., 1988. Material rate dependence and mesh sensitivity on localization problems. Comp. Meth. Appl. Mech. Engng. 67, 69–86.

Nemat-Nasser, S., 1979. Decomposition of strain measures and their rates in finite deformation elastoplasticity. Int. J. Solids Struct. 15, 155–166.

Nemat-Nasser, S., 1982. On finite deformation elasto-plasticity. Int. J. Solids Struct. 18, 857–872.

Pan, W.F., 1997. Endochronic simulation for finite viscoplastic deformation. Int. J. Plasticity 13, 571–586.

Pan, W.F., Chern, C.H., 1997. Endochronic description of viscoplastic behavior of material under multiaxial loading. Int. J. Solids Struct. 34, 2131–2160.

Pan, W.F., Chiang, W.J., Wang, C.K., 1999. Endochronic analysis for rate-dependent elasto-plastic deformation. Int. J. Solids Struct. 36, 3215–3237.

Pan, W.F., Lee, T.H., Yeh, W.C., 1996. Endochronic analysis for finite elastoplastic deformation and application to metal tube under torsion and metal rectangular block under biaxial compression. Int. J. Plasticity 12, 1287.

Ponthot, J.P., 2002. Unified stress update algorithms for the numerical simulation of large deformation elasto-plastic and elasto-viscoplastic processes. Int. J. Plasticity 18, 91–126.

Rashid, M.M., 1993. Incremental kinematics for finite element applications. Int. J. Numer. Meth. Engng. 36, 3937–3956.

Rivlin, R.S., 1981. Some comments on the endochronic theory of plasticity. Int. J. Solids Struct. 17, 231–248.

Rodriguez-Ferran, A., Pegon, P., Huerta, A., 1997. Two stress update algorithms for large strains: accuracy analysis and numerical implementation. Int. J. Numer. Meth. Engng. 40, 4363–4404.

Sandler, I.S., 1978. on the uniqueness and stability of endochronic theories of material behavior. J. Appl. Mech. 45, 263–266.

Simo, J.C., 1988a. A framework for finite strain elastoplasticity based on maximum plastic dissipation and the multiplicative decomposition. Part I: Continuum formulation. Comput. Meth. Appl. Mech. Engng. 66, 199–219.

Simo, J.C., 1988b. A framework for finite strain elastoplasticity based on maximum plastic dissipation and the multiplicative decomposition. Part II: Computational aspects. Comput. Meth. Appl. Mech. Engng. 68, 1–31.

Simo, J.C., Taylor, R.L., 1985. Consistent tangent operator for rate-independent elastoplasticity. Comput. Meth. Appl. Mech. Engng. 48, 101–118.

Valanis, K.C., 1971a. A theory of viscoplasticity without a yield surface. Part I. General theory. Arch. Mech. 23, 517–534.

Valanis, K.C., 1971b. A theory of viscoplasticity without a yield surface, Part II Application to mechanical behavior of metals. Arch. Mech. 23, 535–551.

Valanis, K.C., 1975. On the formulation of endochronic theory of plasticity. Arch. Mech. 27, 857–872.

Valanis, K.C., 1980. Fundamental consequences of a new intrinsic time measure: plasticity as a limit of endochronic theory. Arch. Mech. 32, 171–191.

Valanis, K.C., 1984. Continuum formulation of plasticity. ASME J. Engng. Mater. Technol. 106, 367–375.

Valanis, K.C., Fan, J., 1984. A numerical algorithm for endochronic plasticity and comparison with experiment. Comput. Struct. 19, 717–724.

Valanis, K.C., Peters, J.F., 1991. An endochronic plasticity theory with shear–volumetric coupling. Int. J. Numer. Anal. Meth. Geomech. 15, 77–102.

Valanis, K.C., Read, H.E., 1986. An endochronic plasticity theory for concrete. Mech. Mater. 5, 277–295.

Wang, W.M., Sluys, L.J., de Borst, R., 1997. Viscoplasticity for instabilities due to strain softening and strain-rate softening. Int. J. Numer. Meth. Engng. 40, 3839–3864.

Watanbe, O., Atluri, S.N., 1985. A new endochronic approach to computational elastoplasticity: example of a cyclically loaded cracked plate. J. ASME, Appl. Mech. 52, 857–864.

Watanbe, O., Atluri, S.N., 1986. Internal time, general internal variable and multi-yield surface theories of plasticity and creep: a unification of concepts. Int. J. Plasticity 2, 37.

Wu, H.C., Yip, M.C., 1980. Strain rate and strain-rate history effects on the dynamic behavior of metallic materials. Int. J. Solids Struct. 16, 515–536.

Wu, H.C., Wang, Z.K., Aboutorabi, M.R., 1985. Endochronic modeling of sand in true triaxial test. J. Engng. Mech., ASCE 111, 1257–1276.

Wu, H.C., Ho, C.C., 1995. An investigation of transient creep by means of endochronic viscoplasticity and experiment. ASME J. Engng. Mater. Technol. 117, 260–267.

Wu, H.C., Lu, J.K., Pan, W.F., 1995. Endochronic equations for finite plastic deformation and application to metal tube under torsion. Int. J. Plasticity 32, 1079–1097.